RESEARCH ARTICLE

Key Points:
- The Florida Current surface jet exhibits dominant variability from 3 to 30 days in meandering, core speed, width, and shear
- The jet structure undergoes a robust annual cycle in core speed, width, and shear, corresponding to local wind stress
- The annual cycle of jet transport is very different between 25.5°N and 27°N, likely driven by input from the Northwest Providence Channel

Correspondence to:
M. R. Archer,
matthew.robert.archer@gmail.com

The Surface Velocity Structure of the Florida Current in a Jet Coordinate Frame

Matthew R. Archer[1] 🆔, Lynn K. Shay[1], and William E. Johns[1]

[1]Department of Ocean Sciences, Rosenstiel School of Marine and Atmospheric Science, University of Miami, Miami, FL, USA

Abstract The structure and variability of the Florida Current between 25° and 26°N are investigated using HF radar ocean current measurements to provide the most detailed view of the surface jet to date. A 2-D jet coordinate analysis is performed to define lateral displacements of the jet in time (meandering), and associated structural variations over a 2 year period (2005–2006). In the jet coordinate frame, core speed has a median value of $\sim$160 cm s^{-1} at the central latitude of the array (25.4°N), with a standard deviation (STD) of 35 cm s^{-1}. The jet meanders at timescales of 3–30 days, with a STD of 8 km, and a downstream phase speed of $\sim$80 km d^{-1}. Meandering accounts for $\sim$45% of eddy kinetic energy computed in a fixed (geographical) reference frame. Core speed, width, and shear undergo the same dominant 3–30 day variability, plus an annual cycle that matches seasonality of alongshore wind stress. Jet transport at 25.4°N exhibits a different seasonality to volume transport at 27°N, most likely driven by input from the Northwest Providence Channel. Core speed correlates inversely with Miami sea level fluctuations such that a 40 cm s^{-1} deceleration is associated with a $\sim$10 cm elevation in sea level, although there is no correlation of sea level to jet meandering or width. Such accurate quantification of the Florida Current's variability is critical to understand and forecast future changes in the climate system of the North Atlantic, as well as local impacts on coastal circulation and sea level variability along south Florida's coastline.

1. Introduction

The Florida Current flows through the Straits of Florida, following the continental shelf as it turns from an eastward course along the Florida Keys to a northward course offshore of Miami (Figure 1). Within the Straits, it dominates the ocean circulation, and instabilities and frontal eddies along its shoreward boundary drive upwelling of nutrient-rich waters that stimulate primary productivity (e.g., Archer et al., 2015a; Lee & Mayer, 1977; Lee et al., 1981; Shay et al., 2000; Soloviev et al., 2017). The Florida Current also impacts the ocean and atmosphere at a larger scale, through the poleward transport of heat from the tropics, regulating the regional and global climate (e.g., Yu & Weller, 2007). For these reasons, as well as its convenient proximity to the United States coastline, it is one of the most extensively studied ocean currents in the world, with investigations as far back as the 1800s (Pillsbury, 1890). A number of field campaigns since the 1970s have been specifically targeted at measuring its volume transport (e.g., SYNOPS 71–Duing, 1975; STACS–Molinari et al., 1985; WBTS–Larsen & Sanford, 1985; POFS–Science Applications International Corporation, 1992). Consequently, the Florida Current's mean volume transport and low-frequency variability are now relatively well documented. However, many questions remain regarding its velocity fluctuations and their influence at both the local and basin-wide scales. And until recently, there has been limited capability to study structural variations in the surface jet as it meanders on and off the continental shelf.

In this paper, we use high-frequency (HF) radar to describe the mean Florida Current velocity structure and its variability over a 2 year period (2005–2006). Because the Straits of Florida—with its strong currents and large shears—are a challenging environment for oceanographic sampling, HF radar has several key advantages: it provides 2-D maps of ocean surface currents at high resolution in time (in this study 20 min) and space (1.2 km), can cover large areas (80 × 100 km), operate for years, and avoids the in situ difficulties in such a marine environment. Previous HF radar research in the Straits has utilized these advantages for case studies of short-lived small-scale instabilities that could not be resolved by point measurements or satellite imagery (Archer et al., 2015a; Haus et al., 2000; Parks et al., 2009; Peters et al., 2002; Shay et al., 1998, 2002). However, this is the first time the data are used to precisely quantify the jet velocity structure.
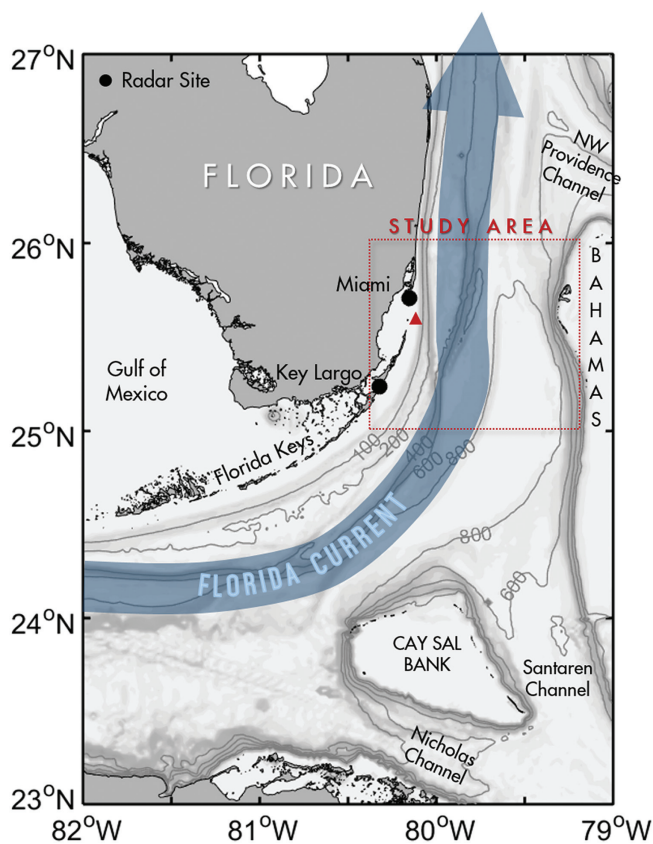
Figure 1. Schematic representation of the Florida Current path through the Straits of Florida, plotted over bathymetry (in meters). Red box denotes the study area, and black circles at Miami and Key Largo denote the location of two HF radar systems used in this study. The tide gauge station is located in Key Virginia (under the black circle labeled Miami). Fowey Rocks meteorological station is denoted by the red triangle. The submarine cable that measures volume transport crosses the Straits at 27°N, at the periphery of this map.

Because the focus of this study is to accurately describe the Florida Current, rather than a patch of ocean, we convert the data to a coordinate frame aligned with the jet—so called "stream" or "jet" coordinates—rather than the typical geographical frame of longitude/latitude. Halkin and Rossby (1985) were the first to apply this method to in situ ocean observations of velocity in the Gulf Stream. They found the temperature and velocity fields were notably "stiff" in jet coordinates; the width and magnitude remained comparatively invariant regardless of the meandering. Furthermore, the eddy kinetic energy (EKE) was reduced by two-thirds, showing that meandering produced significant EKE that accounted for a large portion of the mesoscale eddy activity. Subsequent studies have applied the jet coordinate method to various current systems, using moorings and hydrographic or ADCP sections: in the Gulf Stream (Hogg, 1992; Johns et al., 1995; Rossby & Zhang, 2001), the Kuroshio jet (Hall, 1989; Howe et al., 2009; Waterman et al., 2011), and the Subantarctic Front (Meinen & Luther, 2003; Phillips & Rintoul, 2002). These studies applied the jet coordinate method to derive a horizontal 1-D jet profile in the cross-stream direction. The HF radar used here delivers horizontal 2-D measurements of current velocity that encompass the jet's cross-stream and along-stream structure. By developing an algorithm to work with this 2-D data set, we are able to better quantify the horizontal structural variability of the Florida Current offshore Miami. While two previous studies have also applied a jet coordinate method in the horizontal (Bingham, 1992; Delman et al., 2015), this is the first time that a 2-D jet coordinate analysis has been applied to a remotely sensed gridded data set, in this case HF radar, although the method can be generally applied to any 2-D horizontal data set. Since the method provides time series of the axis position, we also extract statistics on the meandering, core speed, width, surface transport, and lateral shear of the jet.

2. Data and Methods

2.1. Study Area

The area of observation in this study covers 79°W–80.5°W and 25°N–26°N (Figure 1). At this location, the channel has just made the turn to a meridional orientation, and is constrained between Miami to the west, and the Bahamas to the east. The shelf break is located ∼3.5 km offshore of Miami, increasing to a maximum depth of ∼850 m in the channel. Except for the nearshore coastal regions (<10 m water depth) that are forced by wind and tides [Lee & Mayer, 1977], the ocean circulation in the Straits is dominated by the Florida Current and its instabilities, which cover a broad spectrum of temporal and spatial scales (Archer et al., 2015a; Peters et al., 2002). In this paper, our focus is on high-resolution mapping of the jet structure and its variability in time.

2.2. HF Radar Surface Currents

Two 16.045 MHz phased array WERA (WEllen RAdar) radar sites are located in north Key Largo (KL, 25°14.46′N, 80°18.48′W) and Crandon Park on Key Biscayne, Miami (CR, 25°42.84′N, 80°9.06′W) (Figure 2a). Table 1 lists the parameters and capabilities of these systems operating at 16.045 MHz. These WERAs operate in beamforming mode, in which the narrow beam (7.5°–15° azimuth) is electronically steered over the illuminated ocean, with a range resolution of 1.2 km and sampling interval of 20 min.

The conversion from the polar grid to a Cartesian grid is done on the Doppler spectra. For a given Cartesian grid point, the four closest polar grid points are identified (two in range and two in azimuth), weighted by distance, and interpolated onto the Cartesian grid point. Radial velocities are calculated from interpolated
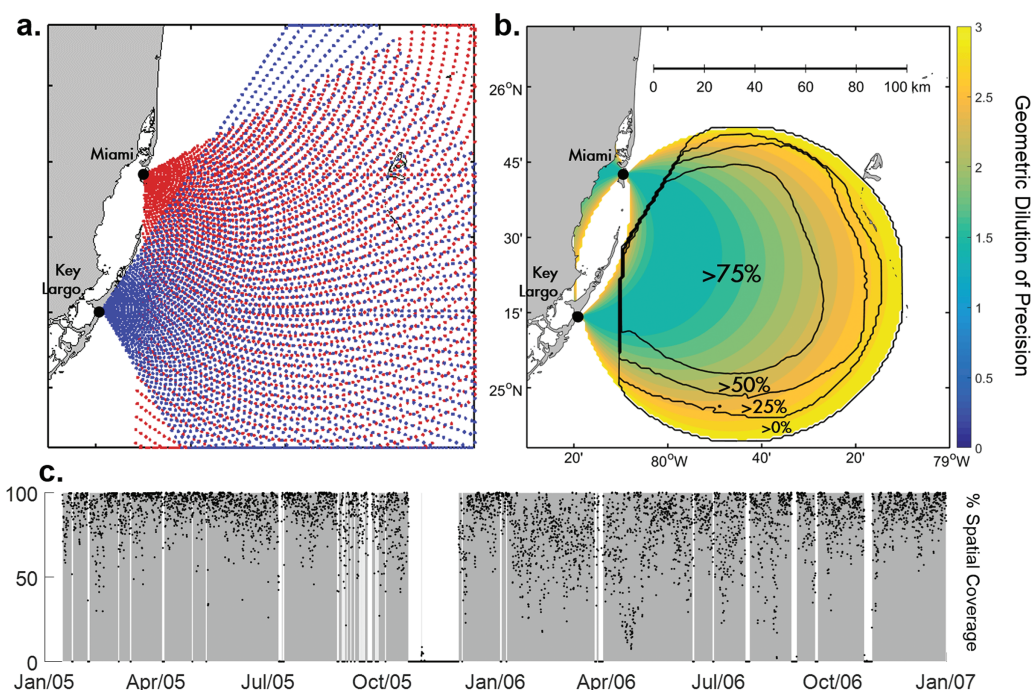
Figure 2. (a) Polar grids for each radar site. (b) Geometric dilution of precision (GDOP) based on the angles of intersection of the radials from each site (filled contours), overlaid with spatial coverage in percent (black contour lines). (c) Time series of percent spatial coverage normalized by maximum footprint from January 2005 to December 2006 (white spaces indicate downtimes when the radar was not operating).

spectra every 20 min (Gurgel et al., 1999). Vector velocities (meridional *v* and zonal *u*) are calculated every 20 min from the radial components, with an unweighted least-squares method (Gurgel, 1994). Radial current accuracy is estimated from the statistics of the velocities within the grid cell (Table 1), and signal-to-noise ratio (Shay et al., 2007). The effect of lateral shear on the accuracy of the radar algorithm within a grid cell is generally less than 4 cm s^{-1} (Parks et al., 2009). Higher sea state, reduced seawater conductivity, and elevated radio interference can reduce the signal-to-noise ratio of the radar, and therefore the range of the foot print (Gurgel et al., 1999). The vector calculation introduces an error due to the geometric dilution of precision (GDOP, Figure 2b, Table 1). The GDOP error is based on the angle of intersection between the radials from each site, and can be thought of as a multiplier of the measurement noise (Chapman et al., 1997). For this reason, the quality control and filtering procedures were conducted on the radial velocities. Grid points were filtered with a 9-point (3 h) Hanning window. Data points that exceeded 3 standard deviations

Table 1
Parameters and Capabilities of the WERA System Operating at 16.045 MHz

Parameters	Value	Capabilities	Value
Operating frequency (MHz)	16.045	Average range (km)	80
Transmit wavelength (m)	18.7	Range cell resolution (km)	1.2
Bragg wavelength (m)	9.35	Measurement depth (m)	0.75
Bragg deep water phase speed (m s^{-1})	3.8	Averaging interval (min)	4.5
Bragg frequency shift (Hz)	0.408	Sampling interval (min)	20
Chirp length (#)	1,024	Max. azimuth resolution (°)	7.5
Chirp duration (s)	0.26	Radial current accuracy (cm s^{-1})	1.8
Modulation bandwidth (KHz)	125	Vector current accuracy (cm s^{-1})	GDOP × RCA[a]
Transmit elements (square array) (#)	4		
Receive elements (#)	16		
Transmitter peak power (W)	30		

[a]RCA = radial current accuracy, GDOP = geometric dilution of precision (Figure 2b).

(STD) from a running 5 day mean, and grid points that exceeded a STD of 50 cm s^{-1}, or with less than 15% data coverage were removed from the analysis.

Data coverage for the 2 year period used in this study was excellent, with spatial coverage consistently greater than 70% of the maximum footprint (Figure 2b). The longest downtime of the radars was a 40 day period in October 2005 after the passage of Hurricane Wilma damaged several of the antennas, otherwise the data gaps were generally less than 1 or 2 days. Comparison with an in situ acoustic Doppler current profiler (ADCP) measuring subsurface currents at a depth of 14 m exhibited root mean square (RMS) differences ~20 cm s^{-1}, consistent with other HF radar comparisons in the Straits of Florida (Archer et al., 2015b; Martinez-Pedraja et al., 2013; Parks et al., 2009; Shay et al., 1998, 2002), and reasonable given the large current magnitudes (>175 cm s^{-1}) and sampling differences between the two instruments (Graber et al., 1997). Such sampling differences include the spatial and temporal averaging intervals, the spatial extent of measurement (radar samples over 1.2 km^2 grid cells, whereas ADCP samples at one point in the *x-y* plane), and consequently the ocean dynamics, including Stokes drift and vertical shear in the velocity profile. In other venues where the ADCP measurements are closer to the surface (~4 m), RMS differences between the radial current measurements range between 2 and 4 cm s^{-1} (Shay et al., 2007). These studies underscore the utility of HF radar measurements of the surface velocity across various coastal regimes.

2.3. Conversion to Jet Coordinates

Converting spatial data that encompasses a meandering current into "jet coordinates" (also termed "stream" or "natural" coordinates) has been shown to improve the time-mean representation of the jet (Halkin & Rossby, 1985). The conversion is made according to the following procedure. First, the location of the jet core and its direction of flow are identified from the axis of maximum velocity. The data points in the surrounding radar domain are then projected onto a coordinate system that is parallel to the jet at its closest location, and the corresponding velocities are rotated into the local downstream and cross-stream directions. Finally, the data are regridded into the new coordinate frame, where the *x* axis is distance from core and the *y* axis is the along-stream position (corresponding to the latitude of the jet core at each point along the axis). Full details of the conversion method may be found in the Appendix A.

3. Results

3.1. Mean Jet Structure in Geographical and Jet Coordinates

The 2 year mean velocity fields in geographical and jet coordinates are presented in Figure 3, in 2-D for both coordinates, and 1-D profiles of cross-stream and downstream components in jet coordinates (based upon 223,153 individual jet cross-sections). The jet coordinate mean has a narrower and more intense core than its geographical counterpart (Figures 3a, 3b, and 3d). The weaker and more diffuse geographical mean is due to the meandering motion of the jet, which spreads the energy over more grid points in time. In 2-D (Figure 3b), the geographical mean also retains the along-stream cyclonic curvature as the jet follows the continental shelf around the Florida peninsula. We can take a closer look at the cross-section of downstream velocity for a single latitude (25.42°S, Figure 3d), to see that the jet coordinate mean has a core speed 16 cm s^{-1} higher than the geographical mean (158 cm s^{-1} compared to 142 cm s^{-1}). The velocity in the core has been redistributed to the flanks, which are higher in the geographical jet, as well as variance caused by the meandering. The difference between these two profiles isolates the effect of time-dependent meandering on the mean current structure. In the jet frame, since the conversion method rotates the velocity vectors to cross-stream and downstream components, the majority of the current speed is put into the downstream component, which is an order of magnitude larger than the cross-stream component (Figures 3c and 3e). The cross-steam velocity is zero at the core of the jet, since by definition the jet core is purely downstream, and across the jet this component stays close to zero in the mean. Downstream velocity has a robust jet profile structure throughout the 2 year period, with a mean core velocity of 158 cm s^{-1}.

In both coordinate systems, the mean cross-stream shear is twice as large in the cyclonic zone than the anticyclonic (Figure 3f). In contrast, the distance of the maximum shear region from the core is significantly shorter in jet coordinates, at ~10 km (cyclonic) and ~20 km (anticyclonic), compared to ~20 and ~40 km, respectively, in geographical coordinates. Also, in jet coordinates the peak cyclonic shear is larger, and the
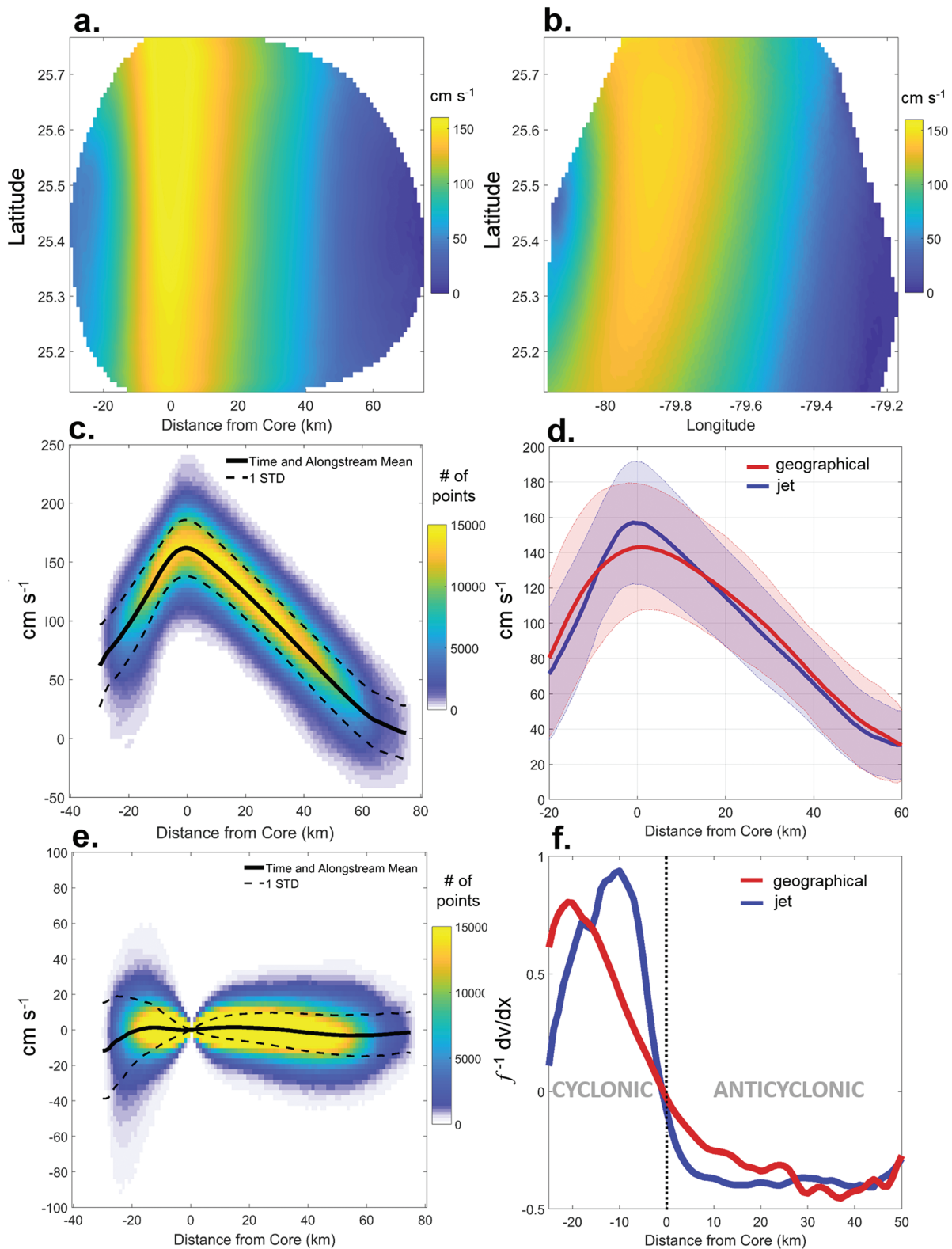
Figure 3. (a) The 2-D jet coordinate 2 year time-mean of current speed; (b) Same but for geographical coordinates; (c) Density contour plot of all observations of the jet's downstream velocity, with the full time and along-stream mean in black, dotted lines one standard deviation. Confidence lines were too close to the mean to plot; (d) Comparison between the geographical and jet frame time-mean at 25.42°N, with shaded regions one standard deviation; (e) The cross-stream velocity in the jet coordinate frame—note that by definition this component of the flow is zero at the core; and (f) Lateral shear (dv/dx) comparison between the geographical and jet frames, normalized by the local Coriolis parameter at 25.42°N.

anticyclonic shear drops rapidly to an almost constant value of $-0.4f$ (where f is the local Coriolis parameter) within 10 km of the jet core.

3.2. Mean Jet Location

The location of the jet core over the 2 year period is presented in Figure 4 as a probability distribution (using 4,072 individual jet axis profiles), and reveals the mode location of the core lies over the $\sim$650 m isobath, 40 km offshore of the Florida coastline (at 25.42°N). The distribution of the jet axis over these 2 years exhibits a longer tail to the east; this is expected since the bathymetry and coastline restricts westward movement of the core. As shown in the 2-D geographical mean (Figure 3b), the jet is still turning cyclonically as it rounds the Florida peninsula, heading north. Path curvature ($\kappa = d^2x/dy^2/(1+(dx/dy)^2)^{3/2}$; not shown) is always positive (0.01 ± 0.001 km^{-1}) and has relatively small variance (standard deviation of 0.006 km^{-2}). As the jet moves northward, it crosses isobaths into shallower water (Figure 4), from 650 to 400 m between 25.2° and 25.65°N.

3.3. Eddy Kinetic Energy

Eddy kinetic energy is defined as EKE $= 0.5(\langle u'^2 \rangle + \langle v'^2 \rangle)$, where u and v represent the u and v-components in either geographical coordinates or jet coordinates, brackets denote a time average, and primes denote a deviation from the time average. A comparison between the two coordinate systems reveals that EKE is reduced in the jet coordinate frame (Figure 5). In this frame, the largest values of EKE are now more tightly constrained along the cyclonic shear zone. In the geographical frame, there is an obvious smearing effect on the EKE, with elevated values over a wider area across the stream, associated with lateral meandering of the jet. Based on the mean values of EKE in each coordinate frame, approximately 45% of the mean EKE field in the geographical frame can be explained by the lateral meandering of the jet.

3.4. Jet Variability

To quantify jet variability, we define the following metrics to describe its structure: meandering (core location), core speed, intensity, surface transport, and width (Figure 6 and Table 2). These variables are defined using the jet coordinate downstream velocity profile at 25.42°N, and filtered with a 40 h Hanning window in time. Meandering denotes the lateral position of the core (identified as maximum downstream velocity) over time, as a displacement from its 2 year mode location, positive (negative) to the east (west) of the mode (this metric is also plotted as a function of longitude and water depth in Figure 7). Core speed is the velocity at the jet's core (i.e., the maximum speed of the jet). Intensity is defined as the difference between the core speed and the average velocity across the jet. This provides a measure of the overall sharpness of
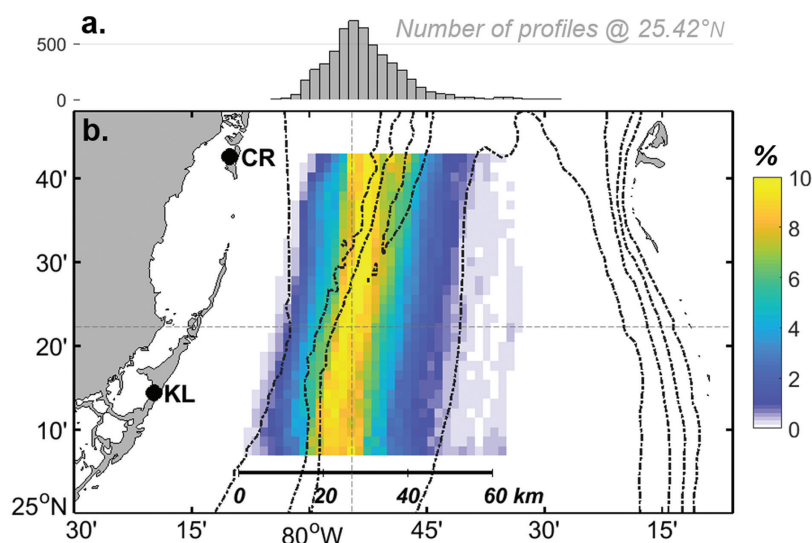

Figure 4. (a) Histogram of core position at 25.42°N. (b) Density contour plot of the jet axis profile for every individual time that the jet core was identified (4,072 profiles). Colored contours display the percent of all observations at each latitude. Isobaths plotted in black dash-dot lines at 200, 400, 600, and 800 m. Dotted lines forming a cross identify the peak of the histogram in Figure 4a with the latitude and longitude in Figure 4b.
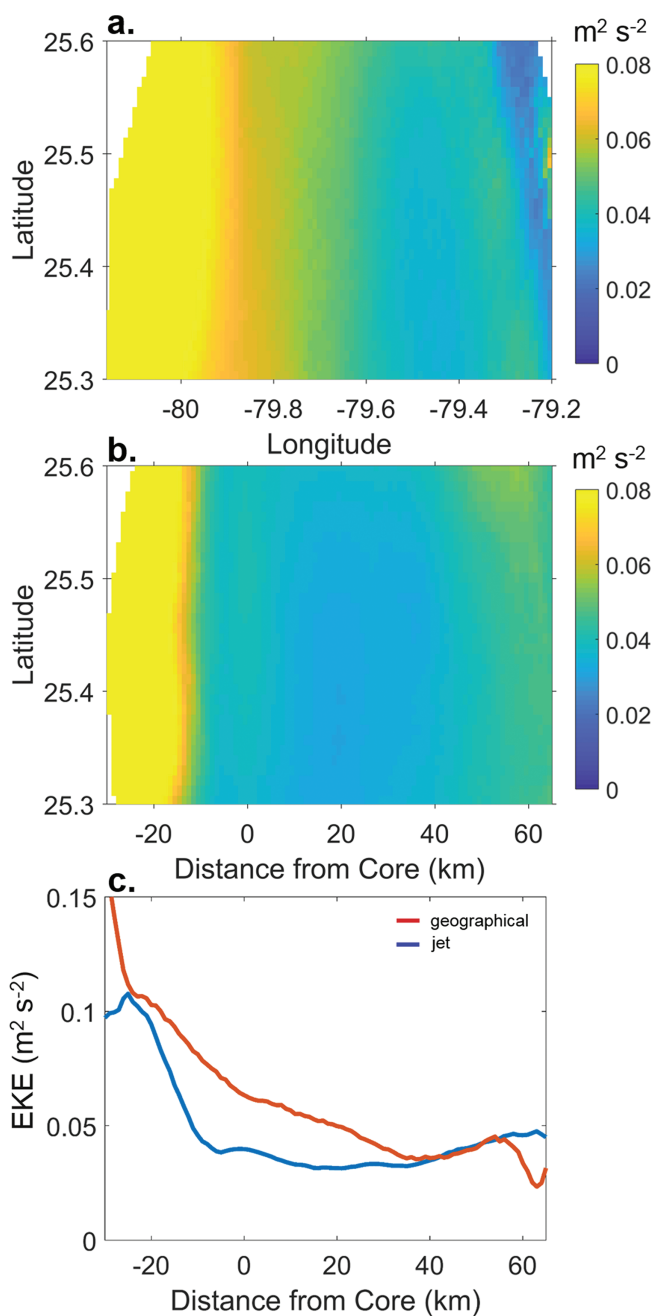
Figure 5. (a) Geographical eddy kinetic energy (EKE); (b) Jet coordinate EKE; and (c) Cross-sectional profiles of EKE at 25.42°N in geographical and jet coordinates. In this figure, the geographical cross-section x axis has been converted to "distance from core" using the maximum value of the jet velocity as the origin.

the jet, and removes the influence of channel-wide fluctuations in the flow, for example associated with local wind forcing (shown later). The term "surface transport" is used hereafter to refer to the surface transport-per-unit-depth ($m^2\ s^{-1}$), calculated by summing up the downstream velocity across the channel for all radar cells. We acknowledge that it is an imperfect measure of the surface transport-per-unit-depth across the full width of the Straits as we are summing velocities over changing spatial coverage; however, the jet core and its flanks are always covered, so the loss of data are mainly along the most outward flanks that do not contribute significantly to the surface transport. We find no correlation between the surface transport and coverage time series (Figure 2c). Width is defined as the distance between the jet "edges," where the edges are 50% of the core speed. The definition is arbitrary, but consistent for the 2 year time series (we originally attempted to use the peak values of lateral shear on each side of the jet but this gave estimates that were too noisy). This width criterion differs from some previous studies that used a threshold velocity value (e.g., Ichikawa et al. (2008) used 20 cm s^{-1} in the Kuroshio), but we believe it provides a more accurate description of the actual jet width variability, by more clearly distinguishing it from the channel-wide fluctuations of the flow. On average, the western edge of the jet is approximately 20 km from the core, while the eastern edge is approximately 40 km from the core. The fluctuations in these edges contribute equally to width changes, with amplitudes of approximately 5 km. This is the first time width changes have been documented in the Florida Current, underscoring the utility of HF radar measurements.

At periods shorter than annual, the core speed of the Florida Current exhibits dominant variability between 3 and 30 days; with a prominent peak at 6 days and between 20 and 30 days (Figure 6a). While these peaks are close to the 95% confidence limits, the same peaks in frequency are exhibited by many of the variables analyzed here. Surface transport, intensity, and width have very similar spectra to core speed. Longer period fluctuations are not evident in the spectrum, but due to the length of data available, we could only investigate periods less than ~100 days. The meandering signal also varies most at periods of 3–30 days (Figure 6b; Johns & Schott, 1987), but with the most prominent peak in the spectrum at 9 days, and smaller peaks at 3, 6, and 20–30 days. These prominent peaks match closely to the local wind stress and volume transport signals, as discussed in section 4.

The jet meanders back and forth over the continental shelf, with a mode position of −79.9°E, where the shelf slope is steepest (the maximum depth gradient in Figure 7c). The maximum offshore meander observed is 40 km east of the mode position, and the westward maximum is 20 km, creating an overall range of 60 km over the 2 year period. This is significantly larger than previous estimates in this region of 5 km (Leaman et al., 1987; Schmitz & Richardson, 1991).

However, the standard deviation is 7.9 km, which agrees more closely with the previous findings. Note that our method provides a direct measure of the meandering, whereas previous studies relied on inference of meandering from point measurements separated typically by tens of kilometers. The three most extreme meanders of the jet occurred on 25 January 2005 (inshore), 19 February 2005 (offshore), and 18 November 2006 (offshore, Figure 7a). During the offshore displacements, the jet was weaker than the inshore case, and characterized by high cyclonic curvature. The inshore displacement was associated with a large anticyclonic eddy east of the jet, akin to the anticyclonic feature investigated by Archer et al. (2015a). The
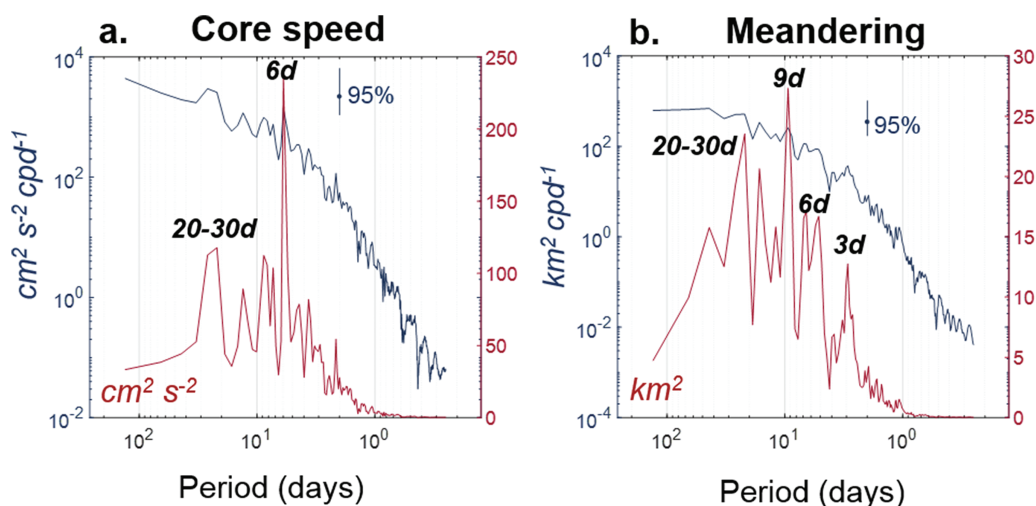
Figure 6. Variance-preserving spectra (red) and power spectra (blue) for (a) Core speed and (b) Meandering. The spectra are calculated using Welch's averaged periodogram method, with 50% overlap and windowed with Hanning weights in the time domain, Fourier transformed, and ensemble averaged. The 95% confidence interval for a chi-squared distribution is plotted on the power axes.

February 2005 offshore displacement was a case study in Parks et al. (2009); they identified it as the downstream expression of a Tortugas gyre (their Figure 14).

To inspect the jet movement in relation to the underlying bathymetry, the time series is plotted as a function of water depth (Figure 7d). Since the continental slope is not linear, and does not deepen uniformly to the east, the transformed time series provides an improved view of the water depth in which the jet predominantly flows. From this point of view, we see the jet sits more frequently over 700 m water depth, with regular movements inshore to depths of around 400 m; and due to the sharp shelf break, the jet does not spend much time over the 500–650 m isobaths. Therefore, with respect to bathymetry, the jet position is bimodal (histogram not shown). However, correlations between this time series of jet water depth (Figure 7d) and other variables provided no additional insight to the meandering time series.

The dominant meander wavelengths and phase speeds can be obtained by calculating the coherence and phase shift between meander time series at two separate latitudes, 25 km apart (Figure 8). For a negative phase shift the northern time series lags that to the south, so meanders at all periods are moving downstream. There is a trend toward larger phase shifts with increasing frequency, indicating the highest frequencies have the shortest wavelengths. Coherence is high (>0.75) for all frequencies, but largest at the longest period meanders. Power spectra reveal dominant meander periods near 3, 6, 9, and 20–30 days (Figure 6b). For a 3 day period meander, the phase shift is 35°, which gives a wavelength (λ) of 250 km and phase speed (c) of 83 km d^{-1}. For a 9 day meander, the phase shift is 12° ($\lambda = 750$ km, $c = 83$ km d^{-1}). A 25

Table 2
Basic Statistics of Jet Variables at 25.42°N

	Mean	Standard deviation	Minimum	Maximum	Integral timescale
Meandering (km)	0 ± 1.7	7.9	-19	42	4
Core speed (cm s^{-1})	157 ± 9	21.5	91	227	9
Width (km)	59 ± 2	6	41	76	16
Surface transport (m^2 s^{-1})	$6{,}320 \pm 356$	918	3,082	8,962	14
Cyclonic shear (normalized by f)	0.5 ± 0.05	0.2	0.07	1.3	6
Anticyclonic shear (normalized by f)	-0.3 ± 0.02	0.09	-0.7	0	6
Intensity (cm s^{-1})	36.6 ± 3.2	10.4	5	96.7	9

Note. Confidence levels are based on a student's *t* distribution and effective degrees of freedom using the integral timescale in days.
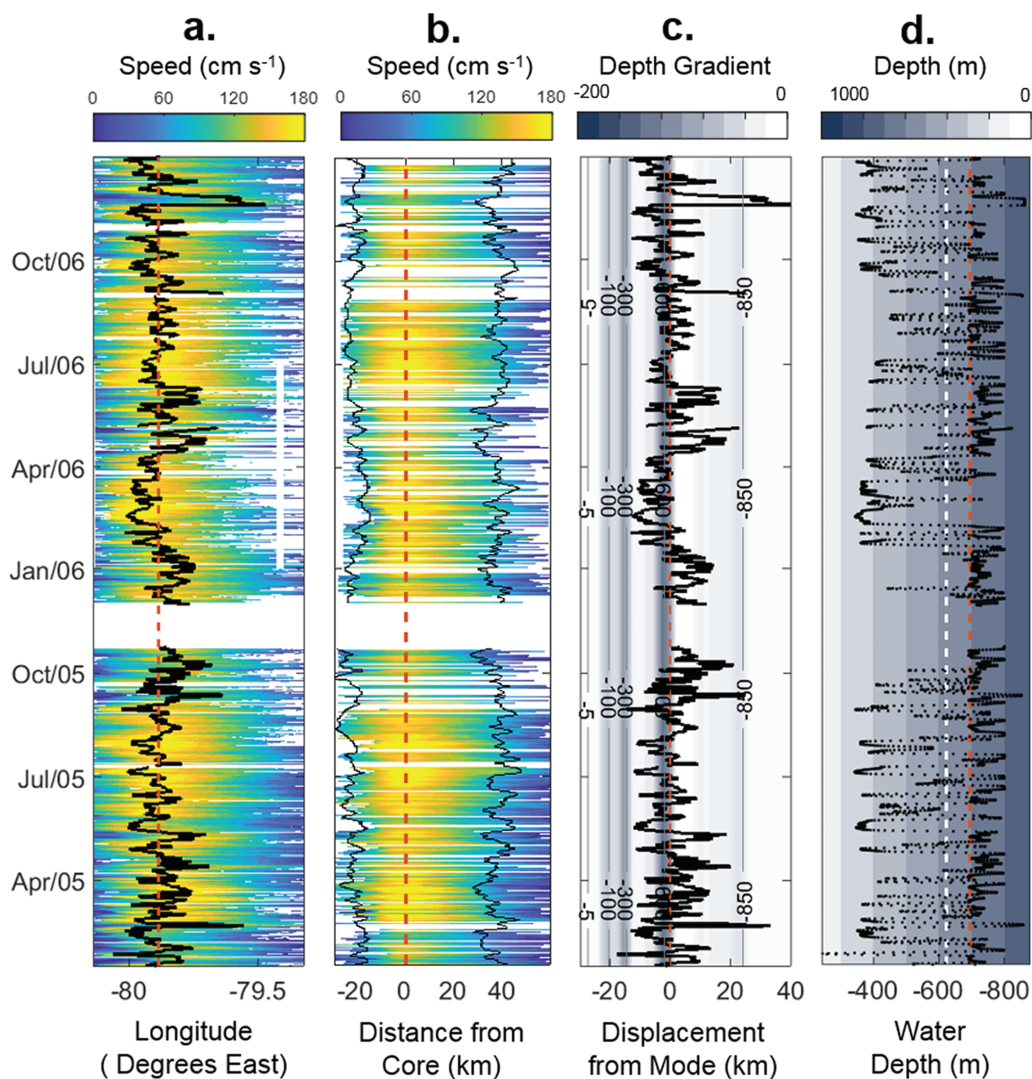
Figure 7. (a) Jet core position at 25.42°N (black line), superimposed on speed (colored contours). Red dashed line is the 2 year mode longitude; (b) Speed plotted in the jet coordinate frame, revealing the fluctuations of the jet when the meandering has been removed. Black lines denote the jet edges defined in section 3.4, red dashed line is core location; (c) Jet core time series plotted as displacement from the mode position (shading represents the gradient of the topography at 25.42°N, with isobaths of 5, 100, 300, 600, and 850 m labeled), red dashed line the new origin (mode position); (d) Jet core time series plotted as a function of water depth. The white line in Figure 7d denotes the 2 year mean jet position in comparison to the median and mode positions (almost identical) in red.

day period meander has a phase shift of 4° ($\lambda = 2,250$ km, $c = 90$ km d^{-1}). At these larger wavelengths of $\mathcal{O}(10^3$ km), the core path variability is more akin to a lateral axis shift than a wave-like meandering motion, as described by Lee and Cornillon (1995). The trend in phase difference over frequency is approximately linear (with the exception of frequencies between 0.15 and 0.25 cycles d^{-1}), which would correspond to a single time delay (Bendat & Piersol, 2010). The time delay is equivalent to 0.31 days, prescribing a nearly constant phase speed of 81 km d^{-1}. This can be interpreted as the meanders moving at approximately the same speed downstream, for all wavelengths.

There is a robust annual cycle in core speed, width, surface transport, and intensity (Figure 9); however, the meandering has no annual signal. The jet's core speed and surface transport show a similar cycle; two peaks, one in late winter and one in the middle of summer, and two minima in spring and fall/early winter. Core speed exhibits a more distinct peak in late winter than surface transport. Intensity also has a peak in late winter, flattening out over the summer, and dipping in August/September both years. Conversely, width peaks in August/September, with the minimum in late winter.
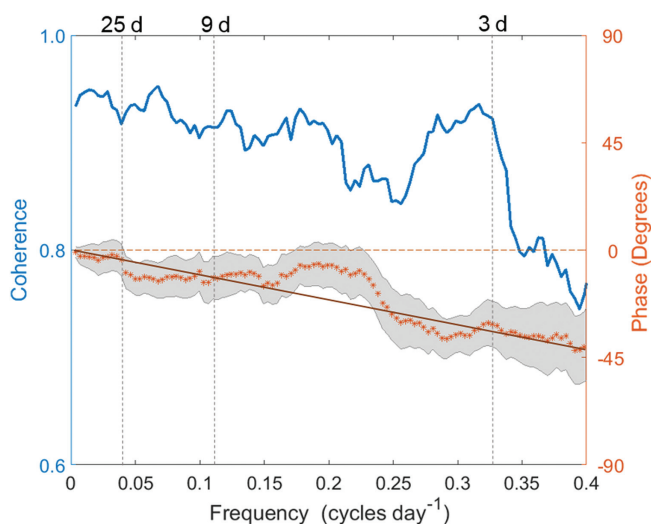
Figure 8. Coherence between two time series of meandering taken at 25.42°N and 25.64°N. An increasingly negative phase shift with higher frequency implies shortening wavelengths. Vertical lines denote the meander periods analyzed for wavelength and phase speed at 25, 9, and 3 days. The red line is a least-squares fit to the phase trend. Gray shading denotes the 95% phase confidence interval based on a Monte Carlo method. The 95% coherence confidence level is 0.39.

3.5. Conditional Jet Averages

Cross-jet profiles of velocity and shear at 25.42°N are conditionally averaged to obtain three composite profiles based on the lowest, middle, and highest one-third of values of each jet metric (Figure 10). These average profiles display more intuitively the effect of each metric on the jet's mean structure. This is done in both the geographical frame (which retains the jet location), and the jet frame (which more accurately represents the jet structure). In the geographical frame, both u and v-components are averaged as each contains a portion of the jet's downstream flow, but not the lateral shear because it is biased (section 3.1); thus, the shear is only presented in the jet frame. We also average the cross-jet profiles by splitting the time series into three randomly selected groups and averaging, and find little to no change in the mean profile (Figure 10f). Furthermore, 1,000 realizations of a case resampling bootstrap (Efron & Tibshirani, 1994) using the jet profile data reveals the robustness of the mean (not shown); the core speed STD over these 1,000 realizations is 0.35 cm s^{-1}.

When the jet is farther offshore, over deeper water, it has a slower core speed, and weaker cyclonic shear (Figure 10a). As the jet moves westward onto the shelf break, the core speed increases by 15 cm s^{-1}, and cyclonic shear doubles from 0.55 to 1.14f. Using core speed as the independent variable to conditionally average the jet, we see the same pattern: the fastest mean jet flows in the shallowest water

(590 m water depth, Figure 10b). In comparison, the slowest jet is 3 km to the east on average—but in 200 m deeper water, which is a significant change given the 800 m depth of the channel. When the jet is faster, the cyclonic and anticyclonic shear zones strengthen, which would be a physical constraint given the limited width of the channel. An interesting finding is that width changes appear to have no relationship to the speed of the jet, with only the shear profile undergoing change between the three cases. Likewise, the position of the jet does not significantly change for different widths (see also Figure 7b). Surface transport increase corresponds to an increasing jet velocity profile (Figure 10d). This is related not only to a strengthening core speed but a channel-wide increase in the velocity—so lateral shear does not change (with the exception of the top one-third case that may be related to width changes). Finally, intensity reveals the nature of its definition—the core speed increases while the flanks remain the same, which creates the largest change in lateral shear seen with these metrics (Figure 10e). Intensity is a satisfactory scalar proxy to describe shear changes across the jet.

4. Relationship to Coastal Sea Level, Volume Transport, and Local Wind

How does the surface jet variability compare to other geophysical variables within the Straits of Florida? To investigate, we analyze independent measurements of coastal sea level, cable-measured volume transport at 27°N, and local wind stress off Miami (see Figure 1 for measurement locations; Table 3 for correlations between the time series). HF radar cross-jet profiles of speed and lateral shear are conditionally averaged as before (i.e., section 3.5 and Figure 10), but now using sea level, transport, and wind as the independent variables (Figure 11).

4.1. Coastal Sea Level

A coastal sea level hourly time series is obtained from Virginia Key tide station in Miami (provided by NOAA's Currents and Tides: http://tidesandcurrents.noaa.gov/). The time series is Hanning filtered with a 40 h window, and subsampled to 3 h intervals to match the jet variables. Comparing to jet speed we see an inverse relationship to the sea level in Miami; the lowest sea level corresponds to the strongest jet, and vice versa (Figure 11a; correlation $r = -0.5$, see Table 3). This correlation with core speed is presumably explained by the hydrographic structure in the channel; for sloping isopycnals in geostrophic balance, a stronger tilt (shoaling to the west, deepening to the east) leads to stronger velocity—and at the surface a depressed (elevated) sea level on the western (eastern) side of the channel. There is no observed relationship between
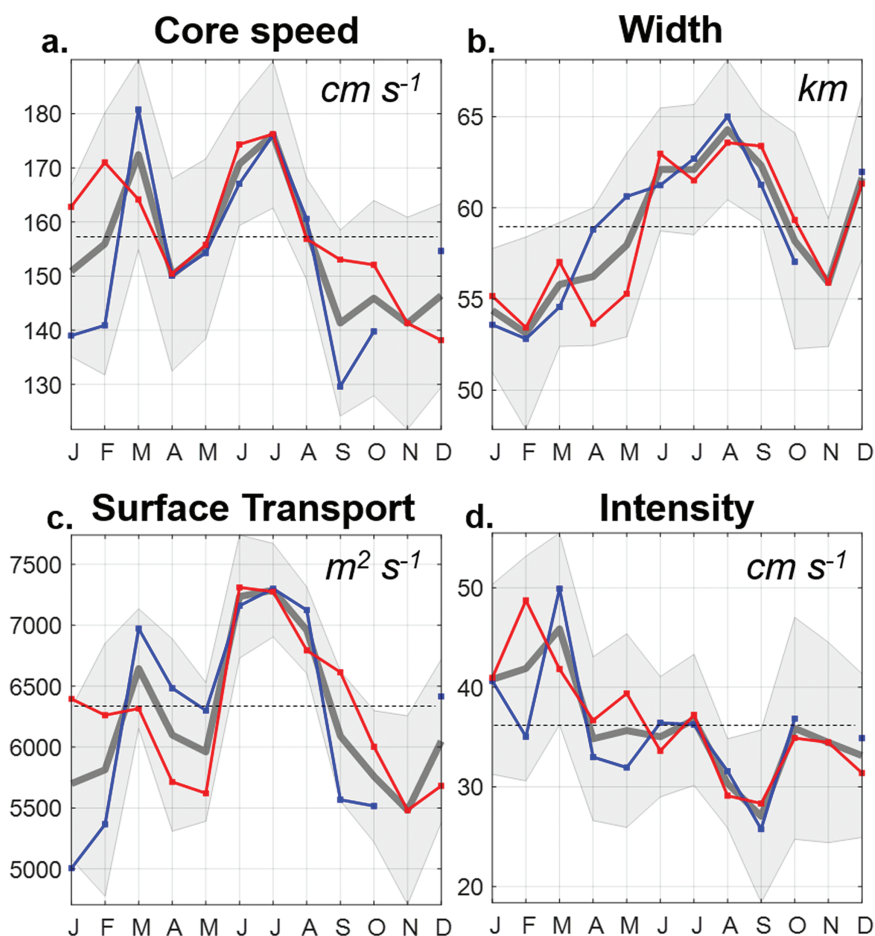
Figure 9. Annual cycle from monthly means for 2005 (blue), 2006 (red), and an overall average (gray). Mean standard deviation of all values for each month shaded in light gray. (a) Core speed; (b) Width; (c) Surface Transport; and (d) Intensity. Dotted lines represent the overall mean.

sea level and meandering, nor width. Surface transport correlates with sea level at $r = -0.45$, and volume transport is correlated at $r = -0.31$ (weaker than surface transport, but still significant at the 99% confidence level). Sea level has an annual cycle that inversely matches core speed and surface transport, with shorter period variance predominantly at 6–7 days, 15–20 days, and 65 days and longer.

4.2. Volume Transport

A volume transport daily time series is obtained from the submarine cable that crosses the channel at 27°N (~175 km north of the radar footprint), which is maintained by NOAA's Atlantic Oceanographic Meteorological Laboratory (www.aoml.noaa.gov/phod/floridacurrent/). As volume transport increases, there is a channel-wide increase in the jet speed, with no evident change in shear. This implies that changes in the depth-integrated flow through the Straits are neither primarily driven by the core speed of the jet, nor width changes, but the total contribution of the channel-wide poleward flow. This can be compared to changes in surface transport, which exhibits similar behavior (Figure 10d, and correlated $r = 0.5$), and core speed, which differs in that it affects shear (Figure 10b and correlated $r = 0.2$). The annual cycle of volume transport is very different between 2005 and 2006, unlike the HF radar jet variables and the sea level fluctuations. This suggests a different forcing mechanism affecting the full depth flow in the channel. At shorter periods, the transport variability peaks at 20 days, with smaller peaks around 6–7 days, 15 days, and 50–80 days.

4.3. Local Wind

Wind data are obtained from the Fowey Rocks meteorological station, located 8 km offshore Miami's Biscayne Bay (25.59°N, 80.1°W; Figure 1), available from NOAA's National Buoy Data Center (http://www.ndbc.
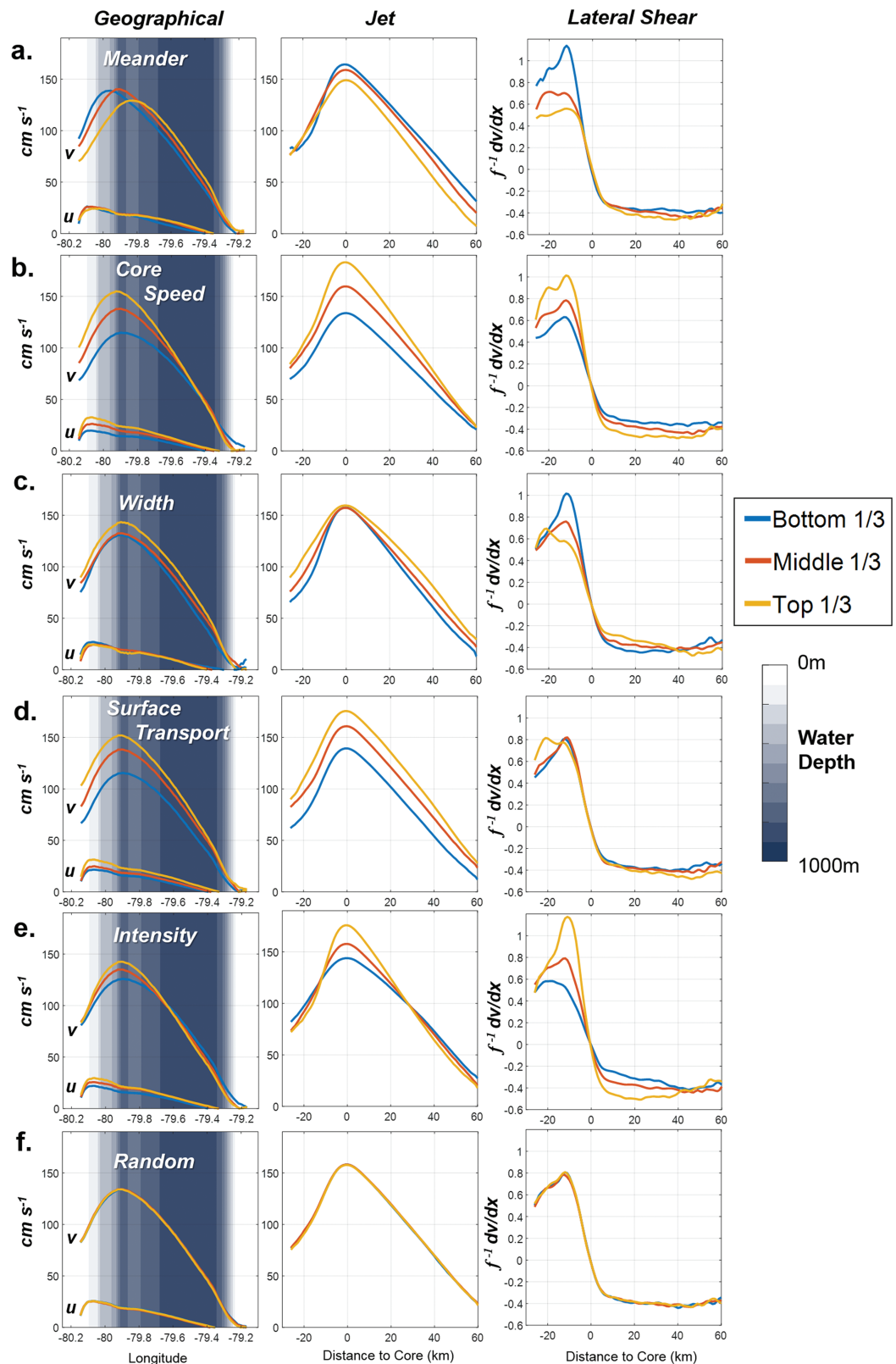
Figure 10. (a)–(f) Conditionally averaged jet profiles based upon the bottom third, middle third, and top third values of the jet metrics labeled in rows. Left column shows the geographical mean cross-jet profile of the *u* and *v*-components, superimposed on the water depth; middle column shows the downstream velocity cross-jet profile in a jet coordinate frame, and the right column shows the lateral shear, also in a jet coordinate frame.

Table 3

Correlations Between Time Series at the 99% Confidence Level, Based on a Normal Distribution Using Effective Degrees of Freedom (Equation (3.15.11a) From Emery & Thomson, 2001)

r0 r Nf	Meandering	Surface transport	Volume transport	Coastal sea level	Meridional wind stress
Core speed	*0.17* **−0.3** 225	*0.3* **0.77** 57	*0.26* **0.4** 89	*0.26* **−0.5** 88	*0.12* **0.35** 446
Surface transport	*0.15* **−0.2** 276		*0.34* **0.5** 52	*0.31* **−0.45** 65	*0.16* **0.46** 228
Volume transport	×	*0.34* **0.5** 52		*0.29* **−0.31** 72	*0.14* **0.25** 295

Note. **r** is the correlation coefficient, r0 is the null hypothesis, and *Nf* is the effective degrees of freedom. The bold values highlight the correlation between variables.

noaa.gov/). Wind stress is calculated as $\tau_y = \rho_a C_D v|U|$, where ρ_a is air density (1.22 kg m^{-3}), C_D is the drag coefficient (1.3 × 10^{-3}), v is the meridional wind velocity, and U is the total wind speed at 10 m. Meridional wind stress, when indexed for negative (southward), near-zero, and positive (northward) values, reveals that it drives a channel-wide increase in jet speed, with no apparent changes in shear. This is the same as for surface transport, but not core speed, which is associated with large shear changes. Because of the highly variable nature of wind stress between positive/negative regimes, the monthly mode of meridional wind stress (Figure 11c) provides a better perspective of the most dominant wind forcing in the region each month. We also plot the mean value of wind stress, which is of much weaker magnitude but shows the same pattern (though not sign; Figure 11c). The annual cycle of wind stress corresponds with that of core speed and surface transport, signifying that when the wind blows south, the jet slows, and as the winds weaken to near-zero and then strengthen to become northward, the jet accelerates. At shorter periods, wind is dominated by fluctuations in the 6–16 day band. Over all periods of variability, wind stress correlates with core speed ($r = 0.35$), surface transport ($r = 0.46$), and volume transport ($r = 0.25$). Zonal wind stress exhibits similar periodicity, but is not discussed further as it shows only a weak annual cycle and no relationship to the jet metrics.

5. Discussion

The mean surface velocity field in jet coordinates shows the Florida Current as a narrow, intense jet that accelerates from south to north by approximately 20 cm s^{-1} (Figure 3a). This seems to be consistent with mass conservation: from south to north the cross-sectional area of the channel decreases almost linearly (from 6 to 4 × 10^7 m^2), and is matched by an increase in the core velocity (from 150 to 170 cm s^{-1}). Additionally, as the jet core moves north it flows into shallower water (Figure 4), which could result in intensification due to vertical compression. The downstream intensification observed is consistent with previous observational studies in the Straits (Laurindo et al., 2017; Leaman et al., 1987; Richardson et al., 1969). Richardson et al. (1969) show a gradual increase of the core speed from ∼140 to ∼180 cm s^{-1} between Key West and the northern exit of the Straits, and similarly Laurindo et al. (2017) show an increase from ∼100 to ∼170 cm s^{-1}. Leaman et al. (1987) obtained a mean core speed of >180 cm s^{-1} at 27°N. As in the radar domain, from the entrance of the Straits to the exit, there is increasing constriction, indicating a required intensification of the current.

The Florida Current surface jet exhibits a consistent annual cycle in its structure, based on the measurements described herein. Core speed peaks between February to March and May to August (∼ +20 cm s^{-1} above its 2 year mean), and dips in September to December (∼ −20 cm s^{-1}). Surface transport (the integral of surface velocity across the Straits) has the same cycle but with a weaker late winter peak, and intensity (the core speed minus the average channel flow) has one major peak in late winter (also exhibited in cyclonic and anticyclonic shear, not shown here), with a minimum in late summer. Width inversely mirrors intensity, with one main peak in late summer and a minimum in late winter. The cycle is consistent between the 2 years, and indicates that as the jet's intensity decreases it widens, and the shear reduces. Local alongshore wind stress reveals a robust annual cycle as well (Figure 11c), with positive (northward) mean values in midsummer, strengthening to negative (southward) during the fall and winter. It also exhibits a small positive increase in late winter. This suggests that local wind stress is the dominant driver of jet variability at the annual period, particularly the summer peak. There are several mechanisms by which local winds can affect the surface currents. Two mechanisms can be explained by Ekman theory (Ekman, 1905). The first is a geostrophic response, whereby a northward wind drives an eastward Ekman transport, leading to divergence (convergence) and upwelling (downwelling) at the western (eastern) boundary; therefore, steepening the east-west tilt of the pycnocline and enhancing northward geostrophic flow (Csanady, 1982; Lee & Williams, 1988). The second is a directly forced surface Ekman effect that could also strengthen the very near-surface flow jet, in which wind-forced currents theoretically move 45° to the right of the wind (in the N.
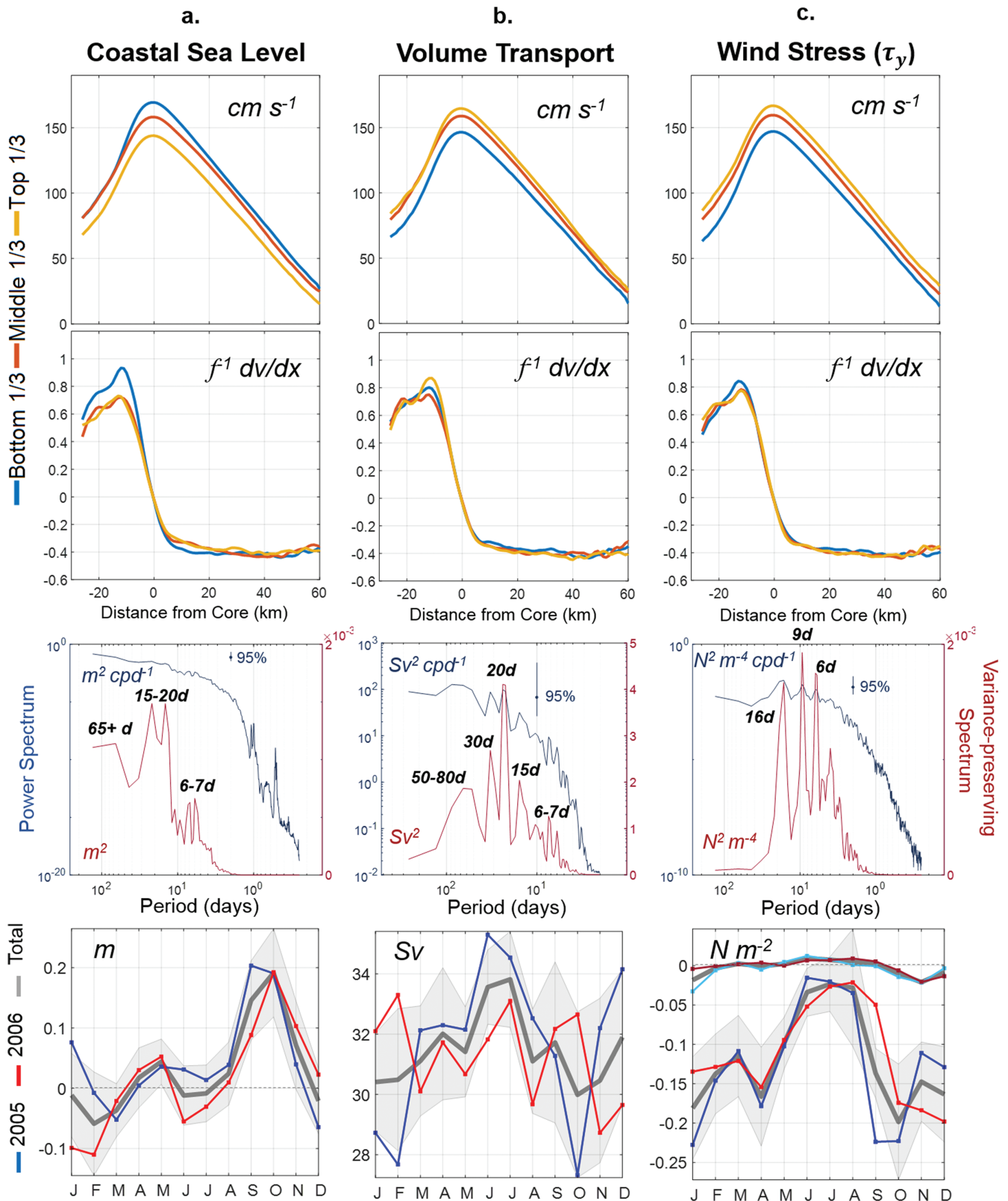
Figure 11. Columns: (a) Coastal sea level; (b) Volume transport; (c) Meridional wind stress. Rows: (row 1) mean jet profile conditionally averaged as per Figure 6; (row 2) lateral shear; (row 3) Power and variance-preserving spectra of the full time series of each variable; and (row 4) Annual cycle (note for the wind stress annual cycle both the monthly mode is plotted (red, blue, grey), and the monthly mean (light blue = 2005; dark red = 2006)).
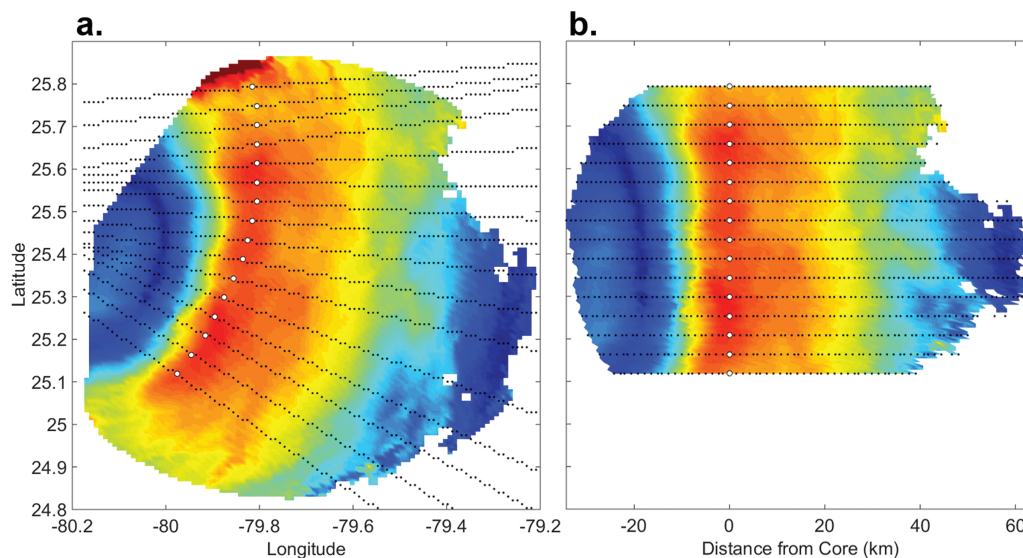
Figure A1. Real data schematic showing jet coordinate conversion, plotted at half-resolution; (a) Geographical coordinate frame (white circles denote the identified core grid points; black dots denote grid points associated with each core point). (b) Jet coordinate frame, the same grid points have been binned relative to distance from core. Note in this new frame the *y* axis signifies the latitude of the core grid point only, while the black grid points may have any original latitude as seen in Figure A1a.

hemisphere). A third contribution from meridional wind stress to the surface flow could be wave-induced Stokes drift, particularly for stronger forcing events (e.g., Kenyon, 1969). Schott et al. (1988) estimated that local wind stress accounts for approximately 22% of the observed seasonal amplitude of volume transport.

It is curious that the late winter peak in jet core speed is nearly as large as the peak that occurs in summer, despite the much weaker alongshore mean wind forcing in winter. While the remote forcing from basin-wide wind stress curl also peaks in late winter, as shown in Figure 16a of Rousset and Beal (2011) (they plot Sverdrup transport averaged over 2001–2006, calculated from the integration of wind stress curl over the Atlantic basin from Africa to the Bahamas along 26°N), the Florida Current is known to be mostly insulated from these interior wind stress curl effects by the steep topography of the Bahamas (Anderson & Corry, 1985; Czeschel et al., 2012). Therefore, it is unlikely that the winter peak in core speed can be attributed to the interior wind forcing, particularly since there appears no time lag between the two. Rousset and Beal (2011) propose this peak may be related to annual weakening of zonal westward winds upstream (offshore Key West, so alongshore in relation to bathymetry) in late winter. However, they struggle to reconcile the Yucatan Current's similar peak in volume transport at this time further upstream (Rousset & Beal, 2010), except to suggest fast communication via barotropic or topographic waves. We speculate there may also be an influence from seasonally varying thermal gradients across the inshore edge of the current. By late winter, inshore waters cool to their minimum temperatures, but the Gulf Stream is continually supplied by warm waters from the south, so that there is an enhanced SST gradient—and with this an expected stronger upper ocean steric height (i.e., sea level) difference—across the front in late winter.

While the jet structure at the surface shows a robust annual cycle driven by seasonal wind stress change, the volume transport measured at 27degN does not; there are major differences between the 2 years. This indicates a possible decoupling between the surface transport and the vertically integrated transport. Part of this could be due to a wider range of dynamic forcing that influences the depth-integrated transport than the surface transport. For instance, Meinen and Luther (2016) showed a lack of coherence in the vertical structure of the Gulf Stream along its entire path, and in the Florida Straits they found little-to-no correlation between the surface and deep flows. The large year-to-year changes in the volume transport annual cycle of the Florida Current over the past few decades has been the focus of several recent papers that have sought to understand why it does not match the seasonal wind fields (e.g., Czeschel et al., 2012; Domingues et al., 2016; Meinen et al., 2010). Domingues et al. (2016) interpret the volume transport's annual cycle by separating the signal into a deterministic (fixed phase) part driven by winds, and a stochastic part driven by westward

propagating sea height anomalies (SHA) from the basin interior, formed in the eastern Atlantic 4–7 years prior (their Figure 1). The interactions between these two mechanisms—either constructive or destructive—lead to amplification or weakening of the annual cycle from year to year. This explains the lack of any annual cycle in the volume transport during 2006, because the SHA pattern during this period acted to reduce the summer wind-driven peak and increase the winter minimum (see Figure 7b of Domingues et al., 2016). That the surface transport at 25.4°N does not exhibit this signal can be attributed to the blocking effect of the Bahamas topography (e.g., Anderson & Corry, 1985). Thus, the difference between surface transport and volume transport is most likely due to the physical separation of the two measurement locations, as 27°N is downstream of the Northwest Providence Channel, so further inputs from the ocean interior can be added to (or subtracted from) the Florida Current transport between these two locations (e.g., Leaman et al., 1995).

We found that sea level fluctuations correlate inversely with the jet's core speed, surface transport, and to a lesser degree, volume transport at 27°N (175 km north). Our work corroborates studies that focus on this aspect of the relationship between the western boundary current and sea level changes along the coast (e.g., Blaha, 1984; Ezer et al., 2013; Maul et al., 1985). Owing to the increasing problems with sea level rise, and more frequent coastal flooding along the SE Florida Coast during the last decade, there is strong interest in both the scientific and local communities to better understand the role of Gulf Stream variability in regional flooding events (Wdowinski et al., 2016). It is noteworthy that jet meandering and width changes are not correlated to coastal sea level fluctuations.

6. Summary

The space-time variability of the Florida Current is resolved in high resolution (1.2 km grid, 3 h sampling), based on HF radar-measured surface currents, to obtain the most detailed representation of the surface jet at 25°–26°N to-date. We transform the 2-D current velocity field at each time step to a jet coordinate frame, thereby removing the smearing effect of meandering on the time-mean structure of the jet. Key results are:

1. The core speed of the jet has a median value of $\sim$160 cm s^{-1} at 25.4°N, with a STD of 35 cm s^{-1} over the 2 year period (2005–2006). Cyclonic shear is twice the magnitude of anticyclonic shear, as predicted by the lateral friction wind-driven ocean circulation model of Munk (1950).
2. The jet accelerates moving northward from 150 to 170 cm s^{-1}, matching an almost linear decrease in channel area, while simultaneously moving across isobaths from 650 to 400 m.
3. In the middle of the domain (25.4°N), the Florida Current follows the shelf edge where the depth gradient is largest, at 650 m, approximately 40 km offshore. It meanders over a range of 60 km, with a STD of 8 km. Meander wavelengths observed are between 250 and 2,250 km, with a nearly constant downstream propagation speed of $\sim$80 km d^{-1}. Meandering accounts for approximately 45% of the EKE field calculated in a fixed geographical frame. The jet has no annual cycle in its position.
4. Core speed exhibits a robust seasonal cycle during the 2 years, with a major peak in summer and second peak in late winter. This matches closely the seasonality of the local meridional wind stress (summer mean peak, and to a lesser degree the late winter peak). The core speed weakens by $\sim$20 cm s^{-1} in the mean when it meanders into deeper water (200 m change) offshore.
5. Jet width exhibits an annual cycle, being maximum in late summer and minimum in late winter. Width changes inversely with the intensity of the jet (a measure of lateral shear between the core and average channel flow), which peaks in the late winter. This is contrary to results downstream that find the Gulf Stream width to be seasonally invariant (Halkin & Rossby, 1985; Rossby & Zhang, 2001). Changes in width do not correspond directly to changes in the jet speed.
6. Volume transport measured by a submarine cable at 27°N is correlated to the surface jet at 25°–26°N (r = 0.5). While it fluctuates at the same periods as the surface jet structure and local wind, it exhibits very different behavior at the annual period, with no consistent cycle in 2005–2006. As a depth-integrated value, it is evidently influenced by a greater variety of processes, including westward propagating sea height anomalies from the east (Domingues et al., 2016). The decoupling between 27°N and 25°–26°N (as well as the upstream Yucatan Current) is most likely driven by additional flow through the Northwest Providence Channel at 26.5°N (e.g., Leaman et al., 1995).

7. Sea level measured at the coast is closely related to the speed of the jet, with a correlation of -0.5 that signifies a weakening jet speed leads to higher sea level at the coast. A linear regression shows that a 10 cm increase in sea level is associated with a $\sim$40 cm s^{-1} decrease in core speed. Sea level is uncorrelated with jet meandering, width changes, or local wind stress.

8. All HF radar-derived jet metrics, as well as the independently measured variables volume transport, sea level, and wind, exhibit the same dominance in variability at timescales between 3 and 30 days.

These high-resolution results provide a useful benchmark for the evaluation of numerical models, as well as the estimates of Florida Current daily frontal position from the National Weather Service. Knowledge of how this jet changes seasonally is of particular interest to ocean users, including the U.S. Coast Guard and local fishermen. By developing the jet coordinate method to work in two dimensions, we have improved the time-averaged representation of the Florida Current. This method can be applied to the continuing HF radar data set to begin assessing whether the Florida Current is changing at a longer timescale relevant to the climate.

Appendix A: Conversion From the Geographical to Jet Coordinate Frame

To convert from geographical to jet coordinates, one must define: (1) the new origin—taken here as the jet core; (2) the jet core's downstream direction; and (3) the cross-stream distance of each grid point from the defined origin. Once these three variables have been determined, the data can be shifted and rotated to the new jet coordinate system.

The Florida Current has a nearly meridional orientation, and its meanders in the HF radar domain are restricted by the channel width. Therefore, it can be reasonably assumed that the core of the Florida Current can be identified at one grid point in longitude (x) for each monotonic step in latitude (y), from the south ($y = 1$) to the north ($y = N$). This method then works iteratively; for each row from $y = 1$ to $y = N$, the core is defined at a point along x. The conversion steps are outlined for a map of velocity vectors at one time step (Figure A1):

1. *Identify the jet core $x_0(y)$*

The jet core is defined as the ridge of maximum velocity (white circles in Figure A1). For each latitude (y), the velocity profile $V(x) = \sqrt{u(x)^2 + v(x)^2}$ is smoothed in longitude by a running 5 point boxcar filter, and the maximum velocity $\hat{V}(x_0)$ is identified as the core x_0. This produces a set of core locations $x_0(y)$. This jet core profile $x_0(y)$ is smoothed using a 1-D spline fit to reduce discontinuities.

2. *Determine the core's downstream direction $\theta(y)$*

The core's downstream direction is computed from the average direction of the velocity vector at the core $\pm$ 3 grid points in x. This produces a set of downstream angles $\theta(y)$ for the set of core locations $x_0(y)$.

3. *At each core location $x_0(y)$, identify the grid points on the map that lie along a line perpendicular to the core downstream direction $\theta(y)$*

For each core location, identify the set of grid points (x, y) that lie along a line nearly perpendicular to the core's downstream orientation $\theta(y)$ (not perfectly perpendicular since we are restricted to equally spaced points on a Cartesian grid). Figure A1 displays the core locations and their associated grid points that lie along the perpendicular line.

4. *For each perpendicular grid point, calculate its distance from the core, and rotate its u-component (v-component) into a cross-stream u_j (downstream v_j) orientation*

Compute the cross-stream distance r (in km) from each perpendicular grid point to its respective core location $x_0(y)$. The new "jet" grid point is a function of cross-stream distance and assigned the core location's latitude (y_c). Rotate the vectors based on the downstream orientation $\theta(y)$:

$$u_j(r, y_c) = u(x, y) \cdot sin(\theta(y)) - v(x, y) \cdot cos(\theta(y)) \tag{1}$$

$$v_j(r, y_c) = u(x, y) \cdot cos(\theta(y)) + v(x, y) \cdot sin(\theta(y)). \tag{2}$$

5. *Regrid data from the geographical grid (x, y) to the jet coordinate grid (r, y_c)*

Bin the grid points according to their cross-stream distance r from the core, and their assigned along-stream location, which is the latitude of their assigned core location (y_c). Thus, the latitude is retained for the

core grid points, while a grid point perpendicular to the core grid point may have any original latitude or longitude (Figure A1). Finally, the data are interpolated onto a uniform grid of 1.2 km spacing in the x direction.

Note this method does not assign every grid point on the map to a core location, as can be seen in Figure A1b. This is because not every grid point lies along a line perpendicular to a core location. After converting to the new coordinate system, the data are quality controlled; again, any data points that exceed 3 standard deviations (STD) from a running 5 day mean are removed, and grid points with less than 30% coverage are thrown away.

At any fixed location in the channel, the measured velocity variability will reflect the time scales of the meandering as well as other possible modes of jet variance. One might expect there to be a longer decorrelation timescale in the jet coordinate frame because the meandering has been removed, leaving only structural changes of the jet. We find the decorrelation timescale is very similar in both coordinate frames, at approximately 10 days. The same result was found previously by Johns et al. (1995), who proposed that the deformation of the frontal structure occurred in association with the meandering, resulting in similar decorrelation timescales for the two coordinate frames. The decorrelation timescale is also the same at points across the stream (not shown), indicating insignificant differences between the core and the two shear zones.

References

Anderson, D. L., & Corry, R. A. (1985). Seasonal transport variations in the Florida Straits: A model study. *Journal of Physical Oceanography*, *15*(6), 773–786. https://doi.org/10.1175/1520-0485(1985)015<0773:STVITF>2.0.CO;2

Archer, M. R., Shay, L. K., Jaimes, B., & Martinez-Pedraja, J. (2015a). Observing frontal instabilities of the Florida Current using high frequency radar. In Y. Liu, et al. (Eds.), *Coastal ocean observing systems*. Amsterdam, the Netherlands: Elsevier. https://doi.org/10.1016/B978-0-12-802022-7.00011-0

Archer, M. R., Shay, L. K., & Martinez-Pedraja, J. (2015b). *Evaluation of WERA HF radar observations: Currents, winds and waves*. In *IEEE/OES 11th Current, Waves and Turbulence Measurements (CWTM)* (pp. 1–9). New York, NY: IEEE. https://doi.org/10.1109/CWTM.2015.7098148

Bendat, J. S., & Piersol, A. G. (2010). *Data Analysis, in random data: Analysis and measurement procedures* (4th ed.). Hoboken, NJ: John Wiley & Sons, Inc. https://doi.org/10.1002/9781118032428.ch11

Bingham, F. (1992). Formation and spreading of subtropical mode water in the North Pacific. *Journal of Geophysical Research*, *97*, 11177–11189. https://doi.org/10.1029/92JC01001

Blaha, J. P. (1984). Fluctuations of monthly sea level as related to the intensity of the Gulf Stream from Key West to Norfolk. *Journal of Geophysical Research*, *89*, 8033–8042. https://doi.org/10.1029/JC089iC05p08033

Chapman, R. D., Shay, L. K., Graber, H. C., Edson, J. B., Karachintsev, A., Trump, C. L., & Ross, D. B. (1997). On the accuracy of HF radar surface current measurements: Intercomparisons with ship-based sensors. *Journal of Geophysical Research*, *102*, 18737–18748. https://doi.org/10.1029/97JC00049

Csanady, G. T. (1982). *Circulation in the coastal ocean* (279 p.). The Netherlands: Springer. https://doi.org/10.1007/978-94-017-1041-1

Czeschel, L., Eden, C., & Greatbatch, R. J. (2012). On the driving mechanism of the annual cycle of the Florida Current transport. *Journal of Physical Oceanography*, *42*(5), 824–839. https://doi.org/10.1175/JPO-D-11-0109.1

Delman, A. S., McClean, J. L., Sprintall, J., Talley, L. D., Yulaeva, E., & Jayne, S. R. (2015). Effects of eddy vorticity forcing on the mean state of the Kuroshio Extension. *Journal of Physical Oceanography*, *45*(5), 1356–1375. https://doi.org/10.1175/JPO-D-13-0259.1

Domingues, R., Baringer, M., & Goni, G. (2016). Remote sources for year-to-year changes in the seasonality of the Florida Current transport. *Journal of Geophysical Research: Oceans*, *121*, 7547–7559. https://doi.org/10.1002/2016JC012070

Duing, W. (1975). Synoptic studies of transients in the Florida Current. *Journal of Marine Research*, *33*(1), 53–73.

Efron, B., & Tibshirani, R. J. (1994). *An introduction to the bootstrap*. Boca Raton, FL: CRC Press.

Ekman, V. W. (1905). On the influence of the earth's rotation on ocean currents. *Arkiv för matematik, astronomi och fysik*, *2*, 1–53.

Emery, W. J., & Thomson, R. E. (2001). *Data analysis in physical oceanography*. Oxford, UK: Pergamon.

Ezer, T., Atkinson, L. P., Corlett, W. B., & Blanco, J. L. (2013). Gulf Stream's induced sea level rise and variability along the US mid-Atlantic coast. *Journal of Geophysical Research: Oceans*, *118*, 685–697. https://doi.org/10.1002/jgrc.20091

Graber, H. C., Haus, B. K., Chapman, R. D., & Shay, L. K. (1997). HF radar comparisons with moored estimates of current speed and direction: Expected differences and implications. *Journal of Geophysical Research*, *102*, 18749–18766. https://doi.org/10.1029/97JC01190

Gurgel, K. W. (1994). *Shipborne measurement of surface current fields by HF radar*. In *Proceedings of Oceans Engineering for Today's Technology and Tomorrow's Preservation (OCEANS'94)* (Vol. 3, pp. III-23–III-27). New York, NY: IEEE. https://doi.org/10.1109/OCEANS.1994.364167

Gurgel, K. W., Antonischki, G., Essen, H. H., & Schlick, T. (1999). Wellen radar (WERA): A new ground-wave HF radar for ocean remote sensing. *Coastal Engineering*, *37*(3), 219–234. https://doi.org/10.1016/S0378-3839(99)00027-7

Halkin, D., & Rossby, T. (1985). The structure and transport of the Gulf Stream at 73 W. *Journal of Physical Oceanography*, *15*(11), 1439–1452. https://doi.org/10.1175/1520-0485(1985)015<1439:TSATOT>2.0.CO;2

Hall, M. M. (1989). Velocity and transport structure of the Kuroshio extension at 35°N, 152°E. *Journal of Geophysical Research*, *94*, 14445–14459. https://doi.org/10.1029/JC094iC10p14445

Haus, B. K., Wang, J. D., Rivera, J., Martinez-Pedraja, J., & Smith, N. (2000). Remote radar measurement of shelf currents off Key Largo, Florida, USA. *Estuarine, Coastal and Shelf Science*, *51*(5), 553–569. https://doi.org/10.1006/ecss.2000.0704

Hogg, N. G. (1992). On the transport of the Gulf Stream between Cape Hatteras and the Grand Banks. *Deep Sea Research Part A: Oceanographic Research Papers*, *39*(7), 1231–1246. https://doi.org/10.1016/0198-0149(92)90066-3

Howe, P. J., Donohue, K. A., & Watts, D. R. (2009). Stream-coordinate structure and variability of the Kuroshio extension. *Deep Sea Research Part I: Oceanographic Research Papers*, *56*(7), 1093–1116. https://doi.org/10.1016/j.dsr.2009.03.007

Ichikawa, K., Tokeshi, R., Kashima, M., Sato, K., Matsuoka, T., Kojima, S., & Fujii, S. (2008). Kuroshio variations in the upstream region as seen by HF radar and satellite altimetry data. *International Journal of Remote Sensing*, *29*(21), 6417–6426. https://doi.org/10.1080/01431160802175454

Johns, W. E., & Schott, F. (1987). Meandering and transport variations of the Florida Current. *Journal of Physical Oceanography*, *17*(8), 1128–1147. https://doi.org/10.1175/1520-0485(1987)017<1128:MATVOT>2.0.CO;2

Johns, W. E., Shay, T. J., Bane, J. M., & Watts, D. R. (1995). Gulf Stream structure, transport, and recirculation near 68°W. *Journal of Geophysical Research*, *100*, 817–838. https://doi.org/10.1029/94JC02497

Kenyon, K. E. (1969). Stokes drift for random gravity waves. *Journal of Geophysical Research*, *74*, 6991–6994. https://doi.org/10.1029/JC074i028p06991

Larsen, J. C., & Sanford, T. B. (1985). Florida Current volume transports from voltage measurements. *Science*, *227*(4684), 302–304. https://doi.org/10.1126/science.227.4684.302

Laurindo, L. C., Mariano, A. J., & Lumpkin, R. (2017). An improved near-surface velocity climatology for the global ocean from drifter observations. *Deep Sea Research Part I: Oceanographic Research Papers*, *124*, 73–92. https://doi.org/10.1016/j.dsr.2017.04.009

Leaman, K. D., Molinari, R. L., & Vertes, P. S. (1987). Structure and variability of the Florida Current at 27°N: April 1982-July 1984. *Journal of Physical Oceanography*, *17*(5), 565–583. https://doi.org/10.1175/1520-0485(1987)017<0565:SAVOTF>2.0.CO;2

Leaman, K. D., Vertes, P. S., Atkinson, L. P., Lee, T. N., Hamilton, P., & Waddell, E. (1995). Transport, potential vorticity, and current/temperature structure across Northwest Providence and Santaren Channels and the Florida Current off Cay Sal Bank. *Journal of Geophysical Research*, *100*, 8561–8569. https://doi.org/10.1029/94JC01436

Lee, T., & Cornillon, P. (1995). Temporal variation of meandering intensity and domain-wide lateral oscillations of the Gulf Stream. *Journal of Geophysical Research*, *100*, 13603–13613. https://doi.org/10.1029/95JC01219

Lee, T. N., Atkinson, L. P., & Legeckis, R. (1981). Observations of a Gulf Stream frontal eddy on the Georgia continental shelf, April 1977. *Deep Sea Research Part A: Oceanographic Research Papers*, *28*(4), 347–378. https://doi.org/10.1016/0198-0149(81)90004-2

Lee, T. N., & Mayer, D. A. (1977). Low-frequency current variability and spin-off eddies along the shelf off Southeast Florida. *Journal of Marine Research*, *35*, 193–220.

Lee, T. N., & Williams, E. (1988). Wind-forced transport fluctuations of the Florida Current. *Journal of Physical Oceanography*, *18*(7), 937–946. https://doi.org/10.1175/1520-0485(1988)018<0937:WFTFOT>2.0.CO;2

Martinez-Pedraja, J., Shay, L. K., Haus, B. K., & Whelan, C. (2013). Interoperability of Seasondes and Wellen radars in mapping radial surface currents. *Journal of Atmospheric and Oceanic Technology*, *30*(11), 2662–2675. https://doi.org/10.1175/JTECH-D-13-00022.1

Maul, G. A., Chew, F., Bushnell, M., & Mayer, D. A. (1985). Sea level variation as an indicator of Florida Current volume transport-Comparisons with direct measurements. *Science*, *227*(4684), 304–307. https://doi.org/10.1126/science.227.4684.304

Meinen, C. S., Baringer, M. O., & Garcia, R. F. (2010). Florida Current transport variability: An analysis of annual and longer-period signals. *Deep Sea Research Part I: Oceanographic Research Papers*, *57*(7), 835–846. https://doi.org/10.1016/j.dsr.2010.04.001

Meinen, C. S., & Luther, D. S. (2003). Comparison of methods of estimating mean synoptic current structure in "stream coordinates" reference frames with an example from the Antarctic Circumpolar Current. *Deep Sea Research Part I: Oceanographic Research Papers*, *50*(2), 201–220. https://doi.org/10.1016/S0967-0637(02)00168-1

Meinen, C. S., & Luther, D. S. (2016). Structure, transport, and vertical coherence of the Gulf Stream from the Straits of Florida to the Southeast Newfoundland Ridge. *Deep Sea Research Part I: Oceanographic Research Papers*, *112*, 137–154. https://doi.org/10.1016/j.dsr.2016.03.003

Molinari, R. L., Wilson, W. D., & Leaman, K. (1985). Volume and heat transports of the Florida Current: April 1982 through August 1983. *Science*, *227*, 295–297. https://doi.org/10.1126/science.227.4684.295

Munk, W. H. (1950). On the wind-driven ocean circulation. *Journal of Meteorology*, *7*(2), 80–93. https://doi.org/10.1175/1520-0469(1950)007<0080:OTWDOC>2.0.CO;2

Parks, A. B., Shay, L. K., Johns, W. E., Martinez-Pedraja, J., & Gurgel, K. W. (2009). HF radar observations of small-scale surface current variability in the Straits of Florida. *Journal of Geophysical Research*, *114*, C08002. https://doi.org/10.1029/2008JC005025

Peters, H., Shay, L. K., Mariano, A. J., & Cook, T. M. (2002). Current variability on a narrow shelf with large ambient vorticity. *Journal of Geophysical Research*, *107*(C8), 3087. https://doi.org/10.1029/2001JC000813

Phillips, H. E., & Rintoul, S. R. (2002). A mean synoptic view of the Subantarctic Front south of Australia. *Journal of Physical Oceanography*, *32*(5), 1536–1553. https://doi.org/10.1175/1520-0485(2002)032<1536:AMSVOT>2.0.CO;2

Pillsbury, J. E. (1890). Gulf stream explorations, observations of currents 1887. In *Report of the Superintendent of U.S. Coast and Geodetic Survey* (Appendix 8, pp. 173–184). Washington, DC: Government Printing Office.

Richardson, W. S., Schmitz, W. J. Jr., & Niiler, P. P. (1969). The velocity structure of the Florida Current from the Straits of Florida to Cape Fear. *Deep-Sea Research and Oceanographic Abstract*, *16*, 225–231.

Rossby, T., & Zhang, H. M. (2001). The near-surface velocity and potential vorticity structure of the Gulf Stream. *Journal of Marine Research*, *59*(6), 949–975. https://doi.org/10.1357/00222400160497724

Rousset, C., & Beal, L. M. (2010). Observations of the Florida and Yucatan Currents from a Caribbean cruise ship. *Journal of Physical Oceanography*, *40*(7), 1575–1581. https://doi.org/10.1175/2010JPO4447.1

Rousset, C., & Beal, L. M. (2011). On the seasonal variability of the currents in the Straits of Florida and Yucatan Channel. *Journal of Geophysical Research*, *116*, C08004. https://doi.org/10.1029/2010JC006679

Schmitz, W. J. Jr., & Richardson, P. L. (1991). On the sources of the Florida Current. *Deep Sea Research Part A: Oceanographic Research Papers*, *38*, S379–S409. https://doi.org/10.1016/S0198-0149(12)80018-5

Schott, F., Lee, T. N., & Zantopp, R. (1988). Variability of structure and transport of the Florida Current in the period range of days to seasonal. *Journal of Physical Oceanography*, *18*, 1209–1230. https://doi.org/10.1175/1520-0485(1988)018<1209:VOSATO>2.0.CO;2

Science Applications International Corporation (1992). *Straits of Florida physical oceanographic field study, final interpretive report: Volume II* (Tech. Rep. OCS Rep. MMS 92-0024, 179 p.). New Orleans, LA: U.S. Department of the Interior, Minerals Management Service, Gulf of Mexico OCS Regional Office.

Shay, L. K., Cook, T. M., Haus, B. K., Martinez, J., Peters, H., Mariano, A. J., . . . Luther, M. (2000). VHF radar detects oceanic submesoscale vortex along Florida coast. *Eos, Transactions American Geophysical Union*, *81*(19), 209–213. https://doi.org/10.1029/00EO00143

Shay, L. K., Cook, T. M., Peters, H., Mariano, A. J., Weisberg, R., An, P. E., & Luther, M. (2002). Very high-frequency radar mapping of surface currents. *IEEE Journal of Oceanic Engineering*, *27*(2), 155–169. https://doi.org/10.1109/JOE.2002.1002470

Shay, L. K., Lee, T. N., Williams, E. J., Graber, H. C., & Rooth, C. G. H. (1998). Effects of low frequency current variability on near-intertial submesoscale vortices. *Journal of Geophysical Research*, *103*, 18691–18714. https://doi.org/10.1029/98JC01007

Shay, L. K., Martinez-Pedraja, J., Cook, T. M., Haus, B. K., & Weisberg, R. H. (2007). High-frequency radar mapping of surface currents using WERA. *Journal of Atmospheric and Oceanic Technology*, *24*(3), 484–503. https://doi.org/10.1175/JTECH1985.1

Soloviev, A. V., Hirons, A., Maingot, C., Dean, C. W., Dodge, R. E., Yankovsky, A. E., . . . McCreary, J. P. (2017). Southward flow on the western flank of the Florida Current. *Deep Sea Research Part I: Oceanographic Research Papers*, *125*, 94–105. https://doi.org/10.1016/j.dsr.2017.05.002

Waterman, S., Hogg, N. G., & Jayne, S. R. (2011). Eddy-mean flow interaction in the Kuroshio extension region. *Journal of Physical Oceanography*, *41*(6), 1182–1208. https://doi.org/10.1175/2010JPO4564.1

Wdowinski, S., Bray, R., Kirtman, B. P., & Wu, Z. (2016). Increasing flooding hazard in coastal communities due to rising sea level: Case study of Miami Beach, Florida. *Ocean & Coastal Management*, *126*, 1–8. https://doi.org/10.1016/j.ocecoaman.2016.03.002

Yu, L., & Weller, R. A. (2007). Objectively analyzed air-sea heat fluxes for the global ice-free oceans (1981–2005). *Bulletin of the American Meteorological Society*, *88*(4), 527–539. https://doi.org/10.1175/BAMS-88-4-527

Erratum